Laser Intensity Stabilization to Control Rydberg Quantum Gates

Bachelor's Thesis

Submitted to the University of Stuttgart by
Jennifer Krauter

July 2021

Examiner: Prof. Dr. Tilman Pfau

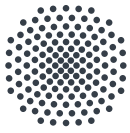

University of Stuttgart
5th Institute of Physics

Pfaffenwaldring 57, 70569 Stuttgart, Germany

Abstract

Lately, quantum gates based on Rydberg atoms increasingly gained interest as a promising way to realize quantum computers. High-fidelity Rydberg quantum gates require precise control over short laser pulses. In this thesis, the feasibility of a system for high-bandwidth pulse shaping using an acousto-optic modulator in combination with an electronic feedback control loop is investigated. The system is characterized and it is shown that a bandwidth of up to 2.5 MHz can be reached.

Zusammenfassung

In den letzten Jahren haben Quantengatter auf der Basis von Rydberg-Atomen als vielversprechende Basis zur Implementierung von Quantencomputern zunehmend an Bedeutung gewonnen. Rydberg-Quantengatter mit hoher Güte erfordern eine präzise Kontrolle über kurze Laserpulse. In dieser Arbeit wird daher ein System zur Pulsformung mit hoher Bandbreite unter Verwendung eines akusto-optischen Modulators in Kombination mit einem elektronischen Regelkreis realisiert. Die Charakterisierung des Systems zeigt, dass eine Bandbreite von bis zu 2.5 MHz erreicht werden kann.

Ehrenwörtliche Erklärung

Ich erkläre hiermit, dass ich die vorliegende Arbeit selbständig verfasst und nur unter Verwendung der angegebenen Quellen und Hilfsmittel angefertigt habe. Alle wörtlich und sinngemäß aus anderen Werken übernommene Aussagen sind als solche gekennzeichnet. Die vorliegende Arbeit war weder vollständig noch in Teilen Gegenstand eines anderen Prüfungsverfahrens. Weiterhin stimmt das elektronische Exemplar mit der gedruckten Version überein.

Stuttgart, den 30.07.2021

Jennifer Krauter

Contents

1 Introduction

In recent years the field of quantum computing and quantum simulation has attracted great interest as a promising way to efficiently solve quantum mechanical calculations. A great number of platforms has been investigated in search for the most successful implementation of a quantum computer including superconductors, quantum dots in semiconductors, trapped ions and photons [1]. Neutral atoms trapped in tweezer arrays represent a promising platform for realizing a quantum computer. The implementation of these arrays is possible in one, two or even three dimensions [2]. As demonstrated in previous quantum simulators [3] and precision measurements [4] trapped neutral atoms can be controlled in large numbers while maintaining excellent quantum coherence.

In particular, the use of Rydberg atoms allows for versatile implementation of quantum gates. Rydberg atoms are atoms in an highly excited state with large principle quantum number. Due to their large radius these atoms are very sensitive to electric fields and show strong long-range interactions. Rydberg quantum gates make use of the Rydberg blockade, which is a result of the strong interaction between two Rydberg states [5]. The realization of Rydberg quantum gates was first proposed at the beginning of this century [6] and then experimentally realized about 10 years ago [7, 8]. In recent advances, Bell state preparations with high gate fidelities of 0.97(3) for alkaline [9] and 0.9951(9) for alkaline earth atoms could be shown [10]. This prospects, that quantum logic gates based on Rydberg atoms will be able to compete with state of the art quantum gates in trapped ions or superconducting systems.

Rydberg quantum gates are implemented by coupling the Rydberg state to one of the qubit states by applying laser pulses. The interactions between trapped Rydberg atom and the surrounding atoms can therefore be precisely controlled. The strong interactions of Rydberg atoms allows for fast gates on the order of 100 ns, which is much faster than the Rydberg lifetimes of approximately 10 µs to 100 µs. The typical gate times for neutral atoms are also distinctively shorter than for trapped-ion qubits. In turn this requires precise control over the applied laser pulses since the precision of the pulse area is directly correlated to the gate fidelity. To compensate for short and long-term drifts an ultra fast active stabilization is therefore necessary. This thesis thus deals with the development of a system for high-bandwidth pulse shaping. The setup consists of an acousto-optic modulator in combination with an electronic feedback loop to stabilize the laser intensity. The limits of this system are probed systematically and the feasibility of achieving the desired bandwidth values between 20 MHz and 50 MHz is tested.

Outline

In order to achieve high-bandwidth laser pulse shaping a system using an acousto-optical modulator in combination with an electronic feedback loop is employed. First, in Chapter 2 the theoretical foundation necessary to understand the applied regulation principle and system used in this thesis is presented. Following this, the details of the optical setup as well as the stabilization circuit are given in Chapter 3. Further, details to the controller unit used in the process are provided. Hereafter, Chapter 4 presents the results of the various measurements. The first aim is to reduce the switching time in acousto-optical modulators, before the approach to reach high-bandwidth laser intensity stabilization is detailed. At the end in Chapter 5, a brief summary of the attained stabilization is given, before different approaches for future improvements are described.

2 Theory

In order to shape light pulses on short time scales an acousto-optic modulator (AOM) is used in combination with a high-bandwidth active feedback loop. The following chapter will therefore provide some details about the theoretical background. Firstly, it deals with the basic theory of control engineering (Sec. 2.1), before the operating principle of a proportional-integral-derivative (PID) controller (Sec. 2.2) is explained, which will be used for the laser intensity stabilization. Afterwards the working principle of an AOM is described (Sec. 2.3) in combination with the theory of Gaussian beams (Sec. 2.4) to obtain a fundamental picture of the optical techniques used in this thesis.

2.1 Control Engineering

The aim in control engineering is to influence dynamic processes and to alter their outcome in a controlled manner. In the following, only a brief introduction into the field of control engineering will be given. The information presented here is based on the more detailed approaches to the theory in [11, 12, 13].

2.1.1 Basic Structure of a Control Loop

The working principle of a feedback control loop is shown in Figure 2.1. Generally, a process is influenced by unknown disturbances and can be regulated using a control variable $u(t)$. External disturbances cause the process variable $y(t)$ to deviate from the setpoint $w(t)$, which represents a boundary condition with a static or dynamic value. This causes

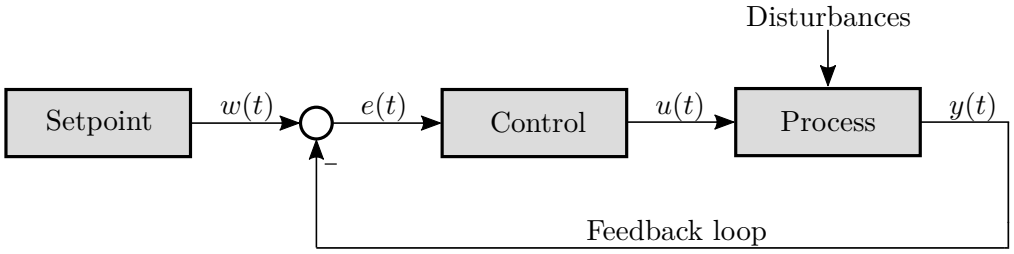

Figure 2.1: Basic principle of a control loop. A process is influence by outer disturbances. The difference between the setpoint $w(t)$ and the process variable $y(t)$ is the error value $e(t)$, which needs to be minimized. The error value $e(t)$ is handed over to the system control, which results in an output of a control variable $u(t)$. This value is then incorporated into the process where it influences $y(t)$.

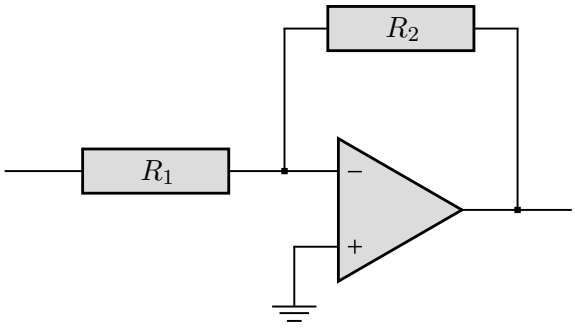

Figure 2.2: Circuit diagram for a proportional control. It consists of two different resistors R_1 and R_2 in combination with an operational amplifier.

an error $e(t)$, which is defined by

$$e(t) = w(t) - y(t), \tag{2.1}$$

to occur. The error $e(t)$ influences the control variable $u(t)$ and thus steers the process in the desired direction. This results in an active feedback on the process variable $y(t)$. In an optimized control loop the difference between the setpoint $w(t)$ and $y(t)$ is minimized in a short time interval. Consequently, the aim is a fast zero convergence of the error $e(t)$.

2.1.2 Proportional Control

A proportional control is a linear feedback system for which the control variable $u_\mathrm{P}(t)$ is proportional to the error $e(t)$

$$u_\mathrm{P}(t) = k_\mathrm{P} \cdot e(t), \tag{2.2}$$

where k_P denotes the linear gain. This is a measure for the magnitude of the system's reaction to an error value and can be calculated using

$$k_\mathrm{P} = \frac{R_2}{R_1} \tag{2.3}$$

with the resistors R_1 and R_2 as shown in the circuit diagram in Figure 2.2. The value of k_P can thus be set by adapting R_1 and R_2.

The transfer function $G(s)$ for a controller, where $s = i\omega$ is the complex frequency, is generally obtained by Laplace transforming $u(t)/e(t)$. For a proportional control the transfer function is given by

$$G_\mathrm{P}(s) = k_\mathrm{P} := \mathcal{L}\left(\frac{u_\mathrm{P}(t)}{e(t)}\right). \tag{2.4}$$

Real proportional controllers are limited by the output limits U_max and U_min. Therefore they only work properly inside a certain range, called the proportional band PB. This is defined as

$$PB = \frac{U_\mathrm{max} - U_\mathrm{min}}{k_\mathrm{P}} \tag{2.5}$$

and is hence directly related to the proportional gain k_P.

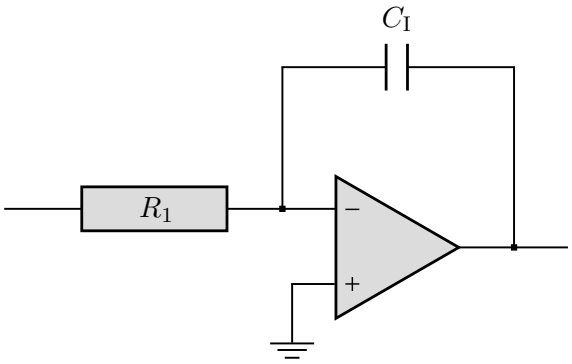

Figure 2.3: Circuit diagram for an integral control. It consists of a resistors R_1 and a capacity C_I in combination with an operational amplifier.

For a proportional control an output is only generated if an error $e(t)$ occurs. This is due to the direct proportionality of the output to the value $e(t)$. Consequently, it is not possible to reach a stable error value $e(t)$ of zero. The remaining error is called offset error, instead the system starts to oscillate. One possible solution of this problem is to incorporate integral action into the overall control.

2.1.3 Integral Control

The control variable $u_\mathrm{I}(t)$ of an integral control depends not only on the current value of the error $e(t)$ but of its past values as well. The corresponding dependency is expressed by

$$u_\mathrm{I}(t) = k_\mathrm{I} \cdot \int_0^t e(\tau)\,\mathrm{d}\tau, \tag{2.6}$$

with the integral gain k_I. This is determined by

$$k_\mathrm{I} = \frac{1}{R_1 \cdot C_\mathrm{I}} \tag{2.7}$$

with resistance R_1 and capacity C_I as shown in Figure 2.3. These parameters can be altered to adjust the integral gain k_I.

The control variable $u_\mathrm{I}(t)$ of an integral control changes until the error $e(t)$ becomes zero eliminating the offset error appearing for a proportional control. The transfer function for this controller type can be expressed as

$$\mathcal{L}\left(\frac{u_\mathrm{I}(t)}{e(t)}\right) =: G_\mathrm{I}(s) = \frac{k_\mathrm{I}}{s}. \tag{2.8}$$

However, a major disadvantage of an integral controller is the comparatively long setting time. This is owing to the fact, that in order for the integral control to generate an output $e(t)$ first has to be present. The longer an error $e(t)$ occurs the larger the response of the integral control, resulting in a better error compensation. Additionally, this type of control is most prone to overshoot. This means the process variable $y(t)$ first exceeds the setpoint $w(t)$ by far. The process variable $y(t)$ then oscillates a couple of times around $w(t)$, before the error $e(t)$ settles to zero.

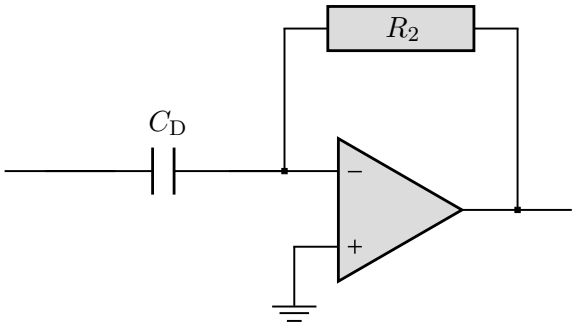

Figure 2.4: Circuit diagram for a derivative control. It consists of a resistors R_2 and a capacity C_D in combination with an operational amplifier.

2.1.4 Derivative Control

This type of control acts proportional to the rate of change of the error $e(t)$ as opposed to the past values like in the integral control. Mathematically, this can be expressed by

$$u_\mathrm{D} = k_\mathrm{D} \cdot \frac{\mathrm{d}}{\mathrm{d}t} e(t), \tag{2.9}$$

where k_D describes the derivative gain. This can be calculated using

$$k_\mathrm{D} = R_2 \cdot C_\mathrm{D}, \tag{2.10}$$

where the resistance R_2 and capacity C_D match to the circuit diagram shown in Figure 2.4. Their values can be used to adapt K_D.

The derivative controller's transfer function can be determined to be

$$\mathcal{L}\left(\frac{u_\mathrm{D}(t)}{e(t)}\right) =: G_\mathrm{D}(s) = k_\mathrm{D} \cdot s. \tag{2.11}$$

Unlike the proportional and the integral control, this sort of control cannot be used individually. The main advantage of a derivative control is that a prediction of subsequent error values $e(t)$ is possible. Thus, changes in the error signal $e(t)$ can be detected and are counteracted early. The controller output $u(t)$ can become quite large for this, as it does not depend on the actual value of $e(t)$. This leads to rapid corrective responses and shorter regulation times.

2.2 Proportional-Integral-Derivative (PID) Controllers

Most of the time control strategies utilizing the above described controller types individually do not lead to sufficient controllers for complex tasks. Thus, in control engineering suitable combinations of different control actions are used for better results. One of the most commonly used structures is that of a PID controller, a combination of proportional, integral and derivative control.

This section will briefly describe the working principle for an idealized PID controller. More accurate descriptions of real PID controllers are discussed in [14, 15], which also form the foundation of the following explanations.

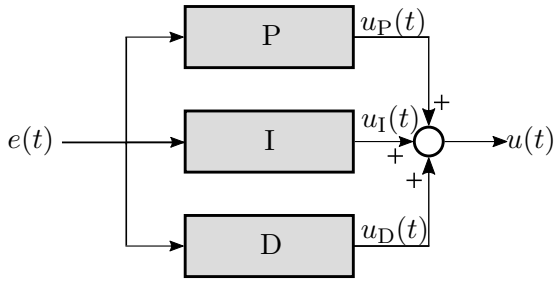

Figure 2.5: Setup of a non-interacting PID controller. The individual components act separately triggered by the value of $e(t)$. Thus the final control variable $u(t)$ is a sum over the three individual values u_P, u_I and u_D.

2.2.1 Working Principle

The output of an idealized PID controller is a sum over its three control components

$$u(t) = \underbrace{k_\mathrm{P} \cdot e(t)}_{\text{proportional}} + \underbrace{k_\mathrm{I} \cdot \int_0^t e(\tau)\,\mathrm{d}\tau}_{\text{integral}} + \underbrace{k_\mathrm{D} \cdot \frac{\mathrm{d}}{\mathrm{d}t} e(t)}_{\text{derivative}}, \tag{2.12}$$

where each component has an individual gain k_P, k_I and k_D. The proportional action ensures that a PID controller can directly react to the error value $e(t)$ and the integral term guarantees that $e(t)$ of a steady state becomes zero. Meanwhile, the derivative term allows to adapt for following error values $e(t)$ and helps the PID controller to act on those accordingly.

Real PID controllers can be divided into two main types depending on their architecture. Figure 2.5 shows a PID with a parallel control circuit. This is also called a non-interacting PID, because each control element works individually. The corresponding transfer function is given by

$$G(s) = k_\mathrm{P} + k_\mathrm{I} \cdot \frac{1}{s} + k_\mathrm{D} \cdot s. \tag{2.13}$$

The second, more common version of PID controllers is the interacting setup, as shown in Figure 2.6. This controller is described with

$$G(s) = k \cdot \left(1 + \frac{1}{T_\mathrm{I} \cdot s}\right)(1 + T_\mathrm{D} \cdot s) \tag{2.14}$$

Generally, the tasks of the single control elements can be distinguished by which time span they act on. The integral control acts on the past, it takes all former error values $e(t)$ into consideration. By only being able to react on the current error $e(t)$ the proportional control is responsible for the present. Lastly, the derivative component analyses the change of the error value $e(t)$ and therefore has influence on the future.

2.2.2 PID Adjustment

In order to achieve a control response which eliminates the error value $e(t)$, it is necessary to adjust the control parameters accordingly. Those include for example the different gain

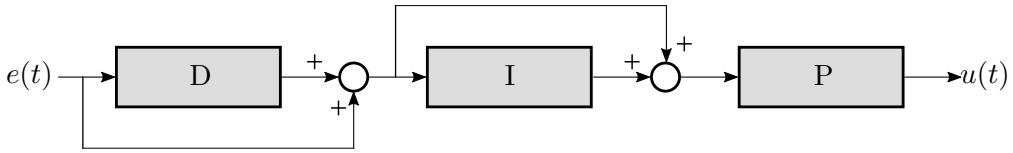

Figure 2.6: Setup of an interacting PID controller. The individual control elements are connected in series and are not longer independent of each other.

values k_P, k_I and k_D. The most important requirement for a PID controller is stability, but often additional conditions like a short rise time or a small overshoot must be fulfilled as well. Real PID controllers are usually more complicated than described in the previous section. However, for this thesis the contemplation of a simplified model is sufficient. The explanations in this section are mainly based on [16], which also provides a more detailed approach.

Firstly, it is important to understand the effect of the individual control actions on the performance of a PID. Therefore, Table 2.1 gives a quick overview of the most important effects when increasing the individual gains k_P, k_I and k_D of the proportional, integral and derivative part.

Keeping the listed effects in mind, a suitable setting for a PID can be found. The Ziegler-Nichols method is a common approach to find a solid starting point for fine tuning [18]. This approach was developed in the 1940s and is based on the simple idea of conducting an experiment to extract process features from the data to find suitable initial parameters. For this purpose, the integral and derivative gain are set to zero before increasing the proportional gain until the system starts to oscillate. This gives the critical gain k_C, as well as the critical oscillation period T_C. The suggested parameters for a PID are then

$$k_\mathrm{P} = 0.6 \cdot k_\mathrm{C} \tag{2.15}$$
$$T_\mathrm{I} = 0.5 \cdot T_\mathrm{C} \tag{2.16}$$
$$T_\mathrm{D} = 0.125 \cdot T_\mathrm{C}. \tag{2.17}$$

While the above settings speed up the response of the control, they also result in a high overshoot. This can be adressed by systematic tuning of the initial set of parameters.

Table 2.1: Individual effects of the proportional, integral and derivative actions in a PID when their corresponding gain k_P, k_I and k_D is increased [17].

Gain	Rise Time	Overshoot	Settling Time	Steady-State Error	Stability
k_P	Decrease	Increase	Small Increase	Decrease	Degrade
k_I	Small Decrease	Increase	Increase	Large Decrease	Degrade
k_D	Small Decrease	Decrease	Decrease	Minor Change	Improve

2.3 Acousto-Optic Modulator (AOM)

Acousto-optic modulators are a most convenient tool in laser modulation. In the following section a short overview on wave propagation in crystals is given to motivate the working principle of AOMs.

2.3.1 Acoustic Waves in Crystals

An acoustic wave is a periodic sound wave which propagates longitudinal or transversal through a medium [19]. Inside a crystal, sound waves lead to atoms vibrating on their lattice sites. This causes the density to locally oscillate, resulting in a time- and space-dependent density. Due to the periodicity of acoustic waves, the density modulation in the crystal is also periodical. As the refractive index n of a crystal is correlated with the material density, the value of n varies periodically throughout the crystal. This consequently leads to light diffraction on the planes of different intensity [20].

2.3.2 Working Principle of an AOM

Based on [21, 22] a short description of AOMs will be given in the following. Figure 2.7 shows the basic setup of an AOM . A transmitter, which is usually realized by a piezo element, sends an ultrasonic wave through a crystal. At the other end an absorber is attached to prevent reflections. The sound waves create periodic density fluctuations in the crystal, where light can be diffracted. The piezo element is powered by an external radio-frequency (RF) driver. This setup can be realized in two different regimes.

Firstly, a distinction between Raman-Nath- and Bragg-diffraction needs to be made. This is achieved by comparing the optical wavelength λ with the acoustic wavelength Λ.

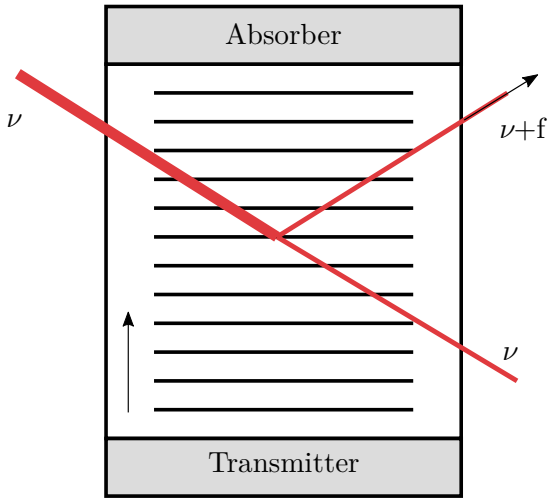

Figure 2.7: In an AOM a transmitter, usually a piezo-electric transducer, creates a sound wave in a crystal. The resulting periodic density modulations in the crystal lead to the diffraction of an incoming light beam of frequency ν. The first diffraction order is Doppler shifted with the frequency f of the sound wave.

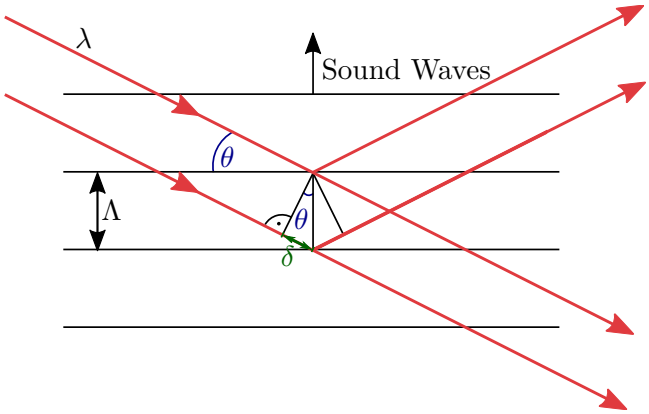

Figure 2.8: Illustration of Bragg's condition. The spacing of the diffraction grating is equivalent to the wavelength Λ of the sound waves. Light with an wavelength λ is diffracted at an angle θ, which is equal to its incidence angle. The lower beam has to cover an additional distance of $2\delta = 2\Lambda \sin(\theta)$ for constructive interference to occur.

If $\lambda d < \Lambda^2$ with the thickness d of the acousto-optical crystal, then the Raman-Nath-regime is achieved, where multiple diffraction orders can be observed. The second regime, which is called Bragg-regime, meets the requirement of $\lambda d > \Lambda^2$. This only diffracts light into the first order, which is why high diffraction efficiencies can be reached for this regime. AOMs mainly operate in the Bragg regime, hence the following explanations concentrate on this principle.

Light diffraction of first order is achieved, if Bragg's condition

$$\sin(\theta) = \frac{\lambda}{2\Lambda}, \tag{2.18}$$

which is illustrated in Figure 2.8, is fulfilled. The incidence angle θ of the light is referenced to the sound wave planes. In order to obtain a diffracted beam an incidence angle is necessary. In an AOM sound waves travel through the crystal, this is why the Doppler effect needs to be taken into account. Due to energy conservation the frequency ν' of the diffracted light wave is modulated to

$$\nu' = \nu \pm f \tag{2.19}$$

with the original frequency ν of the light wave as well as the frequency f of the sound wave. The sign of the modulation depends on the relative propagation direction of the sound to the light wave.

The ratio of diffracted to transmitted light, also known as the diffraction efficiency, is different for every AOM. The intensity I_1 of the first diffraction order is related to the total laser intensity I by

$$\frac{I_1}{I} = \sin^2\left(\frac{M\sqrt{P}}{\lambda}\right) \tag{2.20}$$

with the acoustic power P and the material and geometry-dependent constant M. Consequently, using an AOM enables switching of a laser beam's intensity by modulating the acoustic power.

The switching times in an AOM are bandwidth limited by the used RF driver as well as its inner electrical circuit, which operates the piezo element.

2.4 Gaussian Beams

Laser beams can mathematically be described as Gaussian beams. The following section will present the most relevant properties of Gaussian beams based on the information in [22, 23].

Under the assumption of harmonic time dependency the scalar Helmholtz equation

$$\left(\nabla^2 + \vec{k}^2\right) E = 0 \tag{2.21}$$

can be derived from Maxwell's equations for beams with a wave vector $\vec{k}$ and an electric field component E. Using the time-independent ansatz

$$E(\vec{r}) = A(\vec{r}) \cdot \exp(-ikz) \tag{2.22}$$

for a wave propagating along the z-axis with the complex enveloping function $A(\vec{r})$ and $|\vec{k}| = k$ the approximations

$$\partial_z A(\vec{r}) \ll \frac{A}{\lambda} = \frac{k \cdot A}{2\pi} \approx k \cdot A \tag{2.23}$$

$$\partial_z^2 A(\vec{r}) \ll \partial_z \left(k \cdot A\right) = k \cdot \partial_z^2 A(\vec{r}) < k^2 \cdot A \tag{2.24}$$

can be made, where $\lambda = {}^{2\pi}/_{k}$ is the wavelength. This leads to the paraxial wave equation

$$\nabla_\mathrm{t}^2 A(\vec{r}) - 2ik\partial_z A(\vec{r}) = 0. \tag{2.25}$$

The transversal Laplace operator is defined as $\nabla_\mathrm{t}^2 = \partial_x^2 + \partial_y^2$. This equation is solved either by plane waves, Gaussian beams or higher transverse modes. Gaussian beams are a paraxial approximation of spherical waves. The corresponding electric field component is described by

$$E(\rho, z) = E_0 \frac{w_0}{w(z)} \exp\left(-\frac{\rho^2}{w(z)^2}\right) \exp\left(-ikz - ik\frac{\rho^2}{2R(z)} + i\zeta(z)\right). \tag{2.26}$$

E_0 describes the electric field amplitude at the origin and the cylindrical radius is defined as $\rho^2 = x^2 + y^2$. With $w(z)$ the radius for which the field amplitude falls to $1/e$ of the axial value is denoted. Therefore, $w_0 = w(0)$ is the waist radius, which can be considered the beam's focus point. The curvature radius $R(z)$ describes the wave fronts of the beam, while $\zeta(z)$ is the Gouy phase.

The beam radius $w(z)$ can be expressed as a function of the distance to the beam waist w_0. If the waist is situated at $z = 0$, it can be written as

$$w(z) = w_0 \cdot \sqrt{1 + \left(\frac{z}{z_\mathrm{R}}\right)^2} \tag{2.27}$$

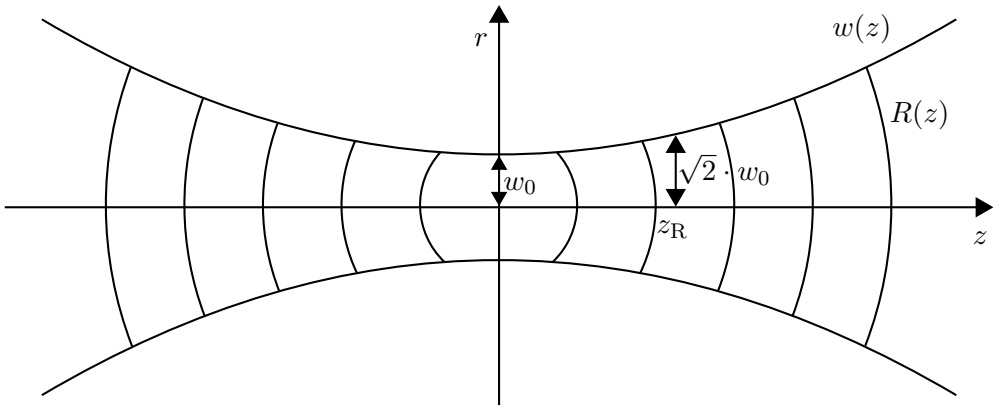

Figure 2.9: Schematic of a Gaussian beam propagating radially symmetric along the z-axis. The illustration shows how the beam radius w changes with distance to the beam waist. Additionally, the Rayleigh length z_R and the curvature radius $R(z)$ are marked.

with the Rayleigh length z_R. This value depends on the wavelength λ and can be determined using

$$z_\mathrm{R} = \frac{\pi \cdot w_0^2}{\lambda}. \tag{2.28}$$

At the Rayleigh length the area of the beam's cross section has doubled compared to the waist position. This can also be used to calculate the curvature of the wavefront via

$$R(z) = z\left(1 + \left(\frac{z_\mathrm{R}}{z}\right)^2\right). \tag{2.29}$$

At the beam waist, this radius becomes infinite as the curvature passes through zero. Lastly, the Gouy phase describes the phase advance of a Gaussian beam compared to a planar wave front. This can be calculated using

$$\zeta(z) = \arctan\left(\frac{z}{z_\mathrm{R}}\right). \tag{2.30}$$

The intensity of a Gaussian beam can be calculated using the relation

$$I(\rho, z) = \frac{1}{2\eta}\left|E(\rho, z)\right|^2, \tag{2.31}$$

where η describes the wave impedance of the medium the beam propagates in. This results in an intensity distribution of

$$I(\rho, z) = I_0\left(\frac{w_0}{w(z)}\right)^2 \exp\left(-\frac{2\rho^2}{w(z)^2}\right) \tag{2.32}$$

with a maximum intensity $I_0 = {}^{2P}/_{\pi w_0^2}$, where P describes the total power of the laser beam. Figure 2.9 further illustrates the above described Gaussian beam propagation along the z-axis.

3 Experimental Setup

The following chapter gives a brief overview of the experimental setup to investigate the feasibility of fast, high-bandwidth pulse-shaping of a laser beam. Starting with a description of the optical setup (Sec. 3.1) the details necessary for the intensity stabilization are explained. Further, the electrical realization of the control loop (Sec. 3.2) is presented

3.1 Optical Setup

The laser in the setup described below operates at a wavelength of $\lambda = 855\,\text{nm}$. However, the principles of the layout will work for laser light of any wavelength, if the optical components are adapted accordingly.

3.1.1 Layout

Figure 3.1 shows the optical setup. Firstly, the laser is coupled into a short, polarization maintaining single-mode fiber to clean the spatial laser mode. Subsequently, the beam passes through two lenses (L1 and L2) composing a telescope to adapt the beam radius from 375 µm to 750 µm. With a third lens (L3), the laser beam is focused into the AOM. Following the AOM the zeroth order laser beam is blocked using a pinhole, only the first order diffracted laser beam is allowed to pass through. This beam then traverses a last

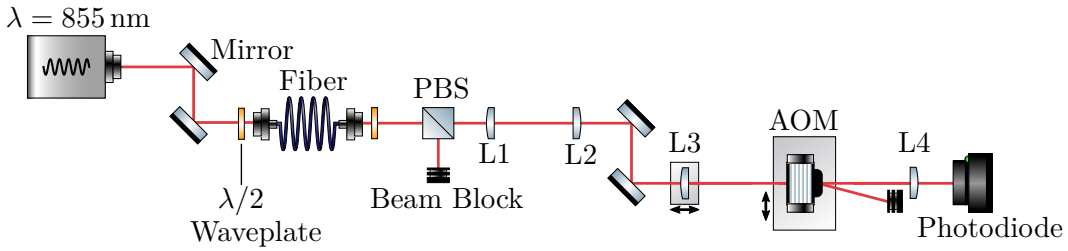

Figure 3.1: Schematic of the optical setup used for the laser intensity stabilization. Lenses L1 and L2 are used to adapt the initial beam radius to 750 µm. The AOM and Lens L3 are mounted on stages, which respectively can be moved along and perpendicular the propagation axis of the laser beam. The direction of the movement is indicated by arrows in the schematic. L3 and L4 together form a telescope, which focuses the laser beam into the AOM and collimates it again afterwards. After passing through the AOM, the transmitted beam is blocked, while the first order diffraction beam is detected using a photodiode.

lens (L4), before being detected using a photodiode, which is connected to the electrical circuit described in Section 3.2.

The AOM is positioned in the focus of lens L3. This leads to the beam waist being directly situated in the acousto-optical crystal. The two lenses L3 and L4 constitute a non-magnifying telescope. This means the focal lengths of both lenses are the same. For better adjustment of the focus point, L3 is mounted on a stage, which can be moved along the propagation axis of the laser beam. The AOM-mounting stage is movable perpendicular to the laser beam. This allows adjusting the distance between the acoustic transducer and the laser beam.

For investigating the feasibility of the high-bandwidth pulse shaping as part of a bigger experiment, a second polarization-maintaining single-mode fiber is required between the last lens and the quantum computer setup. The influence of such an optical fiber will be investigated later on.

3.1.2 AOM Specifications

For the measurements two different AOMs were used. The first one, later called AOM 1, has a center frequency of 80 MHz[1], while the second, later referred to as AOM 2, has a center frequency of 200 MHz [2]. The diffraction efficiency for small beam diameters is noticeably better for AOM 2, as demonstrated by the measurements in Table 4.1. Both AOMs use TeO_2 as an acousto-optical medium. These crystals have an acoustic velocity of $4.2\,\mu m\,ns^{-1}$ [25].

The datasheets of the AOMs provide no information on the dimensions of the used crystals. It was possible to determine the length of the crystal by disassembling an AOM by the same manufacturer with a center frequency of 110 MHz. This was measured to be 11.5 mm and will be of importance later for the investigation of the rise times for both AOMs (Sec. 4.1).

3.2 Stabilization Circuit

The components used for the electronic setup were all chosen to have a high-bandwidths to achieve short stabilization times. First the principal structure of the circuit is explained before a closer look on the properties of the high-bandwidth PID controller is taken.

3.2.1 Electronic Structure

The stabilization circuit shown in Figure 3.2 uses a commercial PID control unit[3]. The red arrows in the figure represent the laser beam, which travels trough the AOM to the photodiode. Here, the intensity is converted into an electric signal. This is then plugged into the inverting input of the PID controller. The non-inverting input is connected to a signal generator, which is used to generate the setpoint. By subtracting both input values

[1] AOMO 3080-122 by Crystal Technology, Inc. [24]
[2] AOMO 3200-1113 by Crystal Technology, Inc. [25]
[3] FALC 110 (Fast Analog Linewidth Control) from Toptica Photonics AG

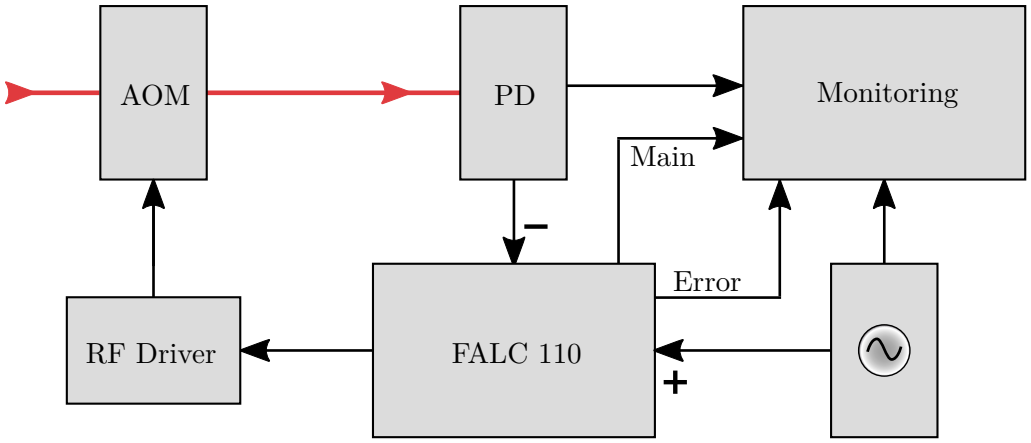

Figure 3.2: Schematic of the stabilization circuit. Red arrows indicate the laser beam while the black ones represent an electrical connection. The photodiode (PD) signal is plugged into the inverting input of the PID controller (FALC 110), while a signal generator is connected to its non-inverting input. In order to control the output power of the RF driver, the output signal $u(t)$ of the control unit is connected to its amplitude modulation input.

the PID controller generates an error value and produces a corresponding output signal, which is handed over to the RF driver.

However, the main output of the PID unit cannot be connected directly to the RF driver since the voltage ranges of both are not compatible. The PID controller's output varies between $-2\,\mathrm{V}$ and $+2\,\mathrm{V}$, while the modulation input level of the RF driver should be set between $0\,\mathrm{V}$ and $1\,\mathrm{V}$. Thus, the signal first goes through a fast, high-conductance diode[4] canceling out any negative voltages before passing a potentiometer, which acts as a voltage divider allowing th ouput to be adjusted to a maximum voltage of $1\,\mathrm{V}$ for the RF driver.

From the driver a signal is conveyed to the AOM. As explained in Section 2.3.2, the diffraction efficiency and therefore the diffracted beam's intensity is related to the acoustic power, hence enabling the stabilization.

For the purpose of measuring the speed and quality of the intensity stabilization several signals are monitored. These include the photodiode signal, the signal of the frequency generator, the error value evaluated by the PID controller and also its main output. This is done using an oscilloscope[5], which has a sufficiently high bandwidth of $1\,\mathrm{GHz}$ to analyze the signals in the range of nanoseconds.

For a fast stabilization it is important, that the components of the circuit are capable of rapid signal transmission. Therefore, the cable lengths are kept short. Furthermore, the

[4] Model 1N4148 by Fairchild Semiconducctor International, Inc. [26]
[5] MDO3104 by Tektronix, Inc. [27]

chosen photodiode[6] has a bandwith of 150 MHz resulting in a rise time just below 7 ns, while the rise and fall time of the RF drivers[7],[8] for both AOMs is specified to be 12 ns.

3.2.2 High-Bandwidth PID Controller

The FALC 110 is a high-speed linear control amplifier applied for laser stabilization [30]. The input section consists of two high-speed differential inputs terminated with 50 Ω. One of these can be used for the setpoint signal, which allows stabilization to a dynamic value. After the input section the FALC 110 has two circuit branches, which carry out the actual control process. This are namely the unlimited integrator branch as well as the Fast ciruit branch. The unlimited integrator branch works comparably slow with a typical bandwidth of only 10 kHz. This is meant to compensate long-time drifts and is therefore not suitable for the stabilization times scale, which are important for pulse stabilization.

The fast circuit branch has a upper bandwidth limit of 50 MHz, which is sufficient to reach stabilization times in the range of a few 10 ns. The fast circuit branch consists of a lead-lag filter, the fast limited differentiator (FLD) and three separate lag-lead filter-stages. These are the extra slow (XSLI), the slow (SLI) and the fast (FLI) limited integrator. With dip switches on the front panel of the FALC 110 unit the individual limits and gain slopes of the filters can be adjusted. Thereby, the transfer function is configured.

[6] PDA 10A-EC by Thorlabs GmbH [28]
[7] 1080-AIFO-1.0 by Crystal Technologies, Inc. [29]
[8] model 1210-AIFO-1.0 from Crystal Technologies, Inc.

4 Results

In an effort to achieve high-bandwidth pulse-shaping of a laser beam multiple limiting factors have to be taken into account. The main limitation to the intensity stabilization is given by the switching time of the AOM (Sec 4.1). Furthermore, the choice of an adequate control unit as well as the transmission delay of the signal in the stabilization circuit plays an important role. The suitability of the chosen PID controller is tested along with the influence of the length of the signal path (Sec. 4.2.)

4.1 Switching Time in an AOM

To attain a high-bandwidth for the intensity stabilization, the switching time of the AOM plays a key role. Two different time periods contribute to the total switching time of an AOM. The initial delay after a signal change is caused by the distance between the acoustic transducer and the laser beam. The sound wave first has to traverse the not illuminated region until the laser beam is reached, before a change in the optical output

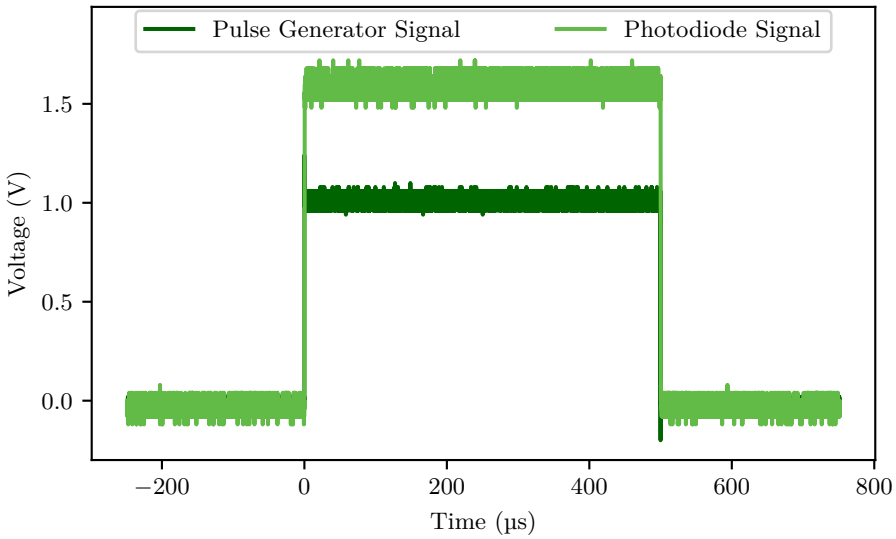

Figure 4.1: Example for the measurement of one pulse to determine the switching time of an AOM. Figure 4.2 shows a zoom on the rising edge of this pulse, were the switching time can be seen. The zero point on the time scale is determined by the rising edge of the pulse generator signal.

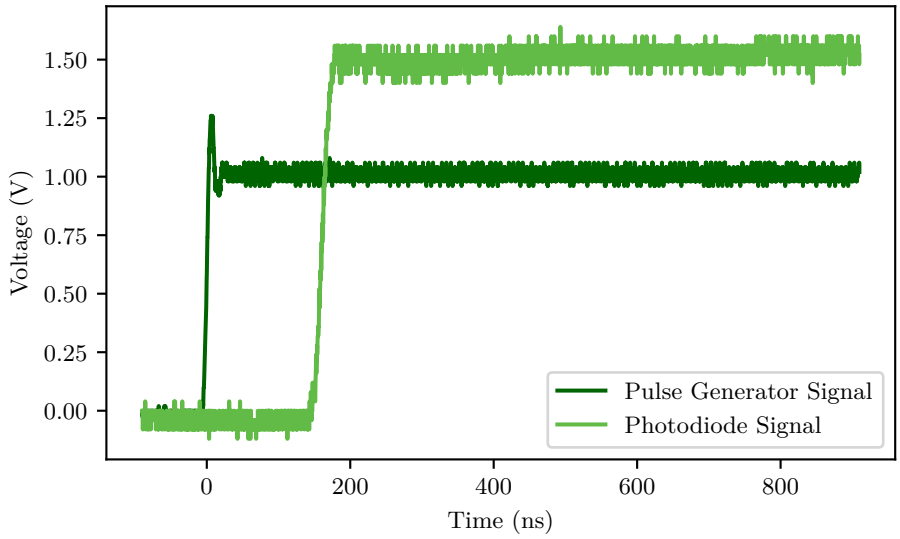

Figure 4.2: Example data for determining the switching time of an AOM. The shown rising edge is a zoom on the pulse depicted in Figure 4.1. The switching time in this case equals 190 ns, which is composed of a 170 ns delay and a rise time of 20 ns.

can be noticed. Another factor contributing to the delay is the switching time of the transducer itself. This static contribution can not be influenced. However, it may vary for AOMs with different center frequencies. The second contribution to the AOM's total switching time is the rise time. The rise time denotes the time difference needed to rise from one amplitude level to another. It is caused by the finite traverse time of the sound wave through the beam.

The velocity of an acoustic wave inside TeO_2 is limited to $4.2\,\mu m\,ns^{-1}$. This factor can be optimized using different acousto-optic media with a higher sound velocity, for example quartz crystals. Though, a disadvantage of this material is the polarization and direction dependency of the sound velocity. For the tests performed in the scope of this thesis, only

Table 4.1: Overview of the focal lenghts f of different lenses and the resulting beam waist w_0 and Rayleigh length z_R used to study the influences on the switching time in both AOMs. The presented switching time is a mean value of the individual values measured for position 1 shown in Figure 4.3 and 4.4, for which the diffraction efficiency is given as well. The values obtained by this method do not represent the optimal switching times reachable for each setting, but are supposed to help identify the overall quality of each setting.

L3 and L4	Waist	Rayleigh Length	Switching Time		Diffraction Efficiency	
f	w_0	z_R	AOM 1	AOM 2	AOM 1	AOM 2
75 mm	45 µm	7.44 mm	156(3) ns	159(3) ns	0.160	0.248
200 mm	75 µm	20.7 mm	136(2) ns	168(6) ns	0.288	0.336

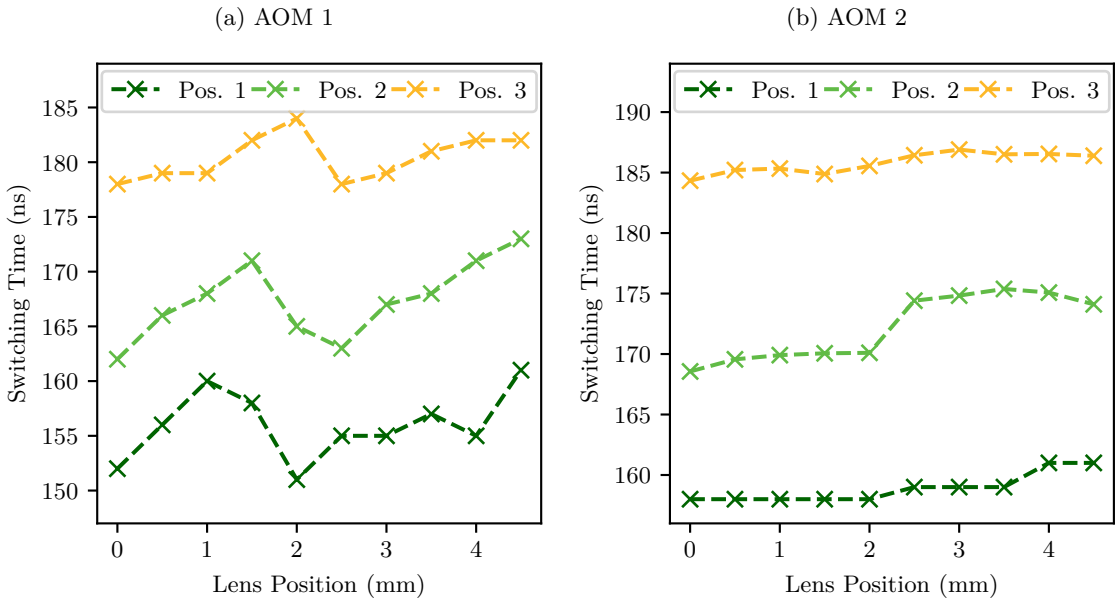

Figure 4.3: Switching times of both AOMs for a beam waist of $w_0 = 45\,\mu m$. The lens position on the x-axis of the diagrams refers to the position of L3 in comparison to its starting point. By adjusting the corresponding stage, the lens is moved in relation to the AOM. This also moves the waist of the laser beam. The three lines correspond to different positions of the respective AOM. Here, position 1 corresponds to the smallest distance between acoustic transducer and laser beam. This distance is increased in 50 µm steps for each position.

AOMs with TeO_2 were available. Therefore a further inspection of sound velocity effects could not be conducted.

The first measurements examine the effect of the distance between the acoustic transducer and the laser beam as well as the beam's radius for two different AOMs. The information obtained from this process is used to determine the AOM better suited for the stabilization measurements. The investigations described in this section concentrate only on the switching time in the AOMs and are consequently conducted independent of the controller unit. This setup is realized by connecting the RF driver of the AOM directly to the signal generator described in Section 3.2.

The following procedure is conducted using both AOMs (Sec. 3.1.2) in turn. The signal generator is used to modulate a rectangular pulse with an amplitude of 1.0 V onto the RF driver, which then issues maximum output power. The intensity of the first diffraction order of the laser beam is measured via a photodiode read out by an oscilloscope, which is also used to observe the output from the signal generator. Figure 4.1 shows an example for the measurement of one pulse. The amplitude on the photodiode exceeds the amplitude of the driving pulse, because there is no active feedback involved. This does not further matter for determining the switching time. In Figure 4.2 a zoom on the rising edge of the same pulse is shown. For this configuration the delay amounts to 170 ns, while the rise

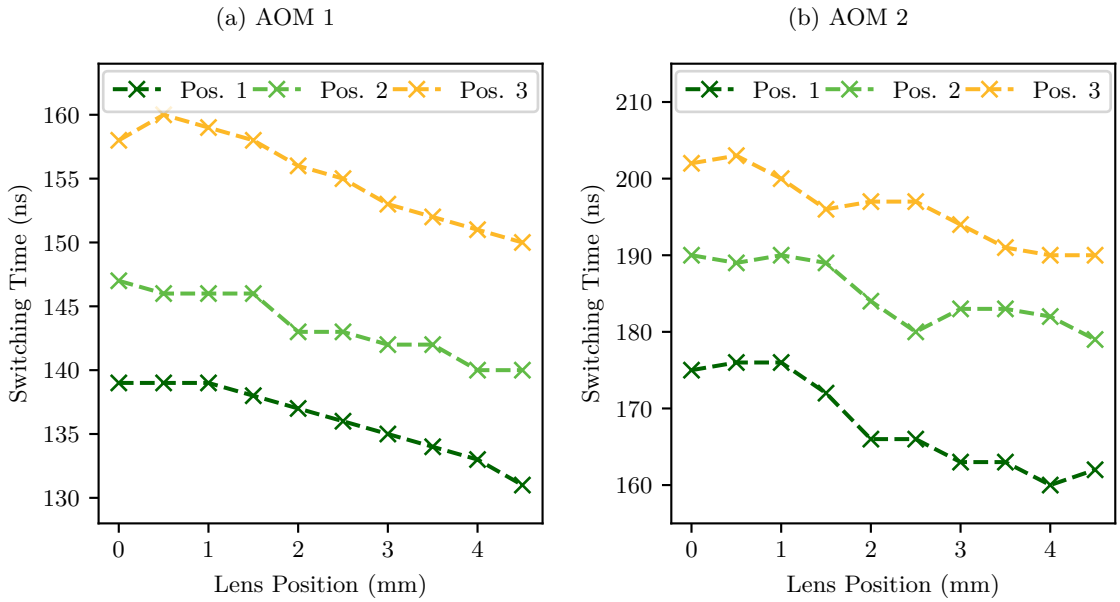

Figure 4.4: Switching times of both AOMs for a beam waist of $w_0 = 75\,\mu m$. The lens position on the x-axis of the diagrams refers to the position of L3 in comparison to its starting point. By adjusting the corresponding stage, the lens is moved in relation to the AOM. This also moves the waist of the laser beam. The three lines correspond to different positions of the respective AOM. Here, position 1 corresponds to the smallest distance between acoustic transducer and laser beam. This distance is increased in 50 µm steps for each position.

time is approximately 20 ns. This results in a total switching time of about 190 ns. The following evaluations of the switching time were done more precisely using the functions of the oscilloscope.

As discussed in Section 3.1, the lenses L3 and L4 are chosen with equal focal lengths and therefore compose a non-magnifying telescope. Depending on the choice of focal length the beam waist in the AOM, located between both lenses, can be adjusted. L3 is mounted on a translation stage, which can be moved parallel to the propagation direction of the laser beam. Consequently, it is possible to fine adjust the position of the focal point in reference to the AOM. The AOM itself is also mounted on a translation stage, which is used to alter its transversal position with respect to the laser beam and thus the distance between the acoustic transducer in the AOM and the laser beam.

Table 4.1 gives a compact overview of the different combinations investigated in the following measurements. First, lenses with a focal length of $f = 75\,mm$ were used. This results in a beam waist $w_0 = 45\,\mu m$ in the focus plane. Using equation (2.28) the Rayleigh length can be calculated to

$$z_R = \frac{\pi \cdot (45\,\mu m)^2}{855\,nm} = 7.44\,mm. \tag{4.1}$$

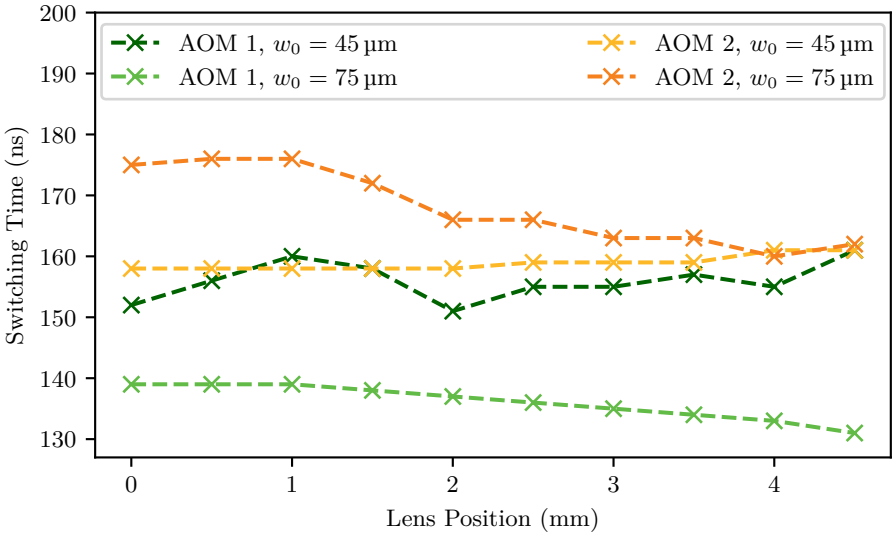

Figure 4.5: Switching times of both AOMs for different beam waists. The lens position on the x-axis refers to the position of L3 in comparison to its starting point. By adjusting the corresponding stage, the lens is moved with respect to the AOM. This also moves the waist of the laser beam inside the AOM crystal.

Results for this measurement are illustrated in Figure 4.3. Here, the switching time is plotted against the lens position, which equals different waist positions of the laser beam. This is done for three different distances between the acoustic transducer and the laser beam for both AOMs. Position 1, which equals the smallest distance, was chosen in a way, that enough light was diffracted into the first order to obtain a good signal to noise ratio for all measurements. From that on, the transducer-beam distance was increased by 50 µm for each of the three settings. The switching time in AOM 2 is generally more stable respective to the lens position but slower than for AOM 1. It can also be seen, that with increasing distance between transducer and laser beam the switching time rises approximately by the expected value of

$$t_{\text{Delay}} = 4.2\,\mu\text{m}\,\text{ns}^{-1} \cdot 50\,\mu\text{m} = 21\,\text{ns}. \tag{4.2}$$

The measurements described above are repeated for lenses with focal length $f = 200\,\text{mm}$. In this case the beam waist was measured to $w_0 = 75\,\mu\text{m}$, which prompts a Rayleigh length of $z_\text{R} = 20.7\,\text{mm}$. Figure 4.4 shows the results of the measurements. The decreasing slope of the lines indicates, that the lens position is not well adjusted and that the beam waist is not directly in the acousto-optical medium during the measurement. Since AOM 1 already shows a significantly lower switching time than in the first case, it was not necessary to redo the measurements, when this error was detected. Additionally, for the final stabilization setup different lenses were used, for which the alignment was then adjusted more properly.

The data shows clearly that AOM 1 again has a faster switching time. The switching time increases as before with the distance of the laser beam to the transducer. For an overall comparison of the different beam radii with both AOMs, Figure 4.5 shows the switching

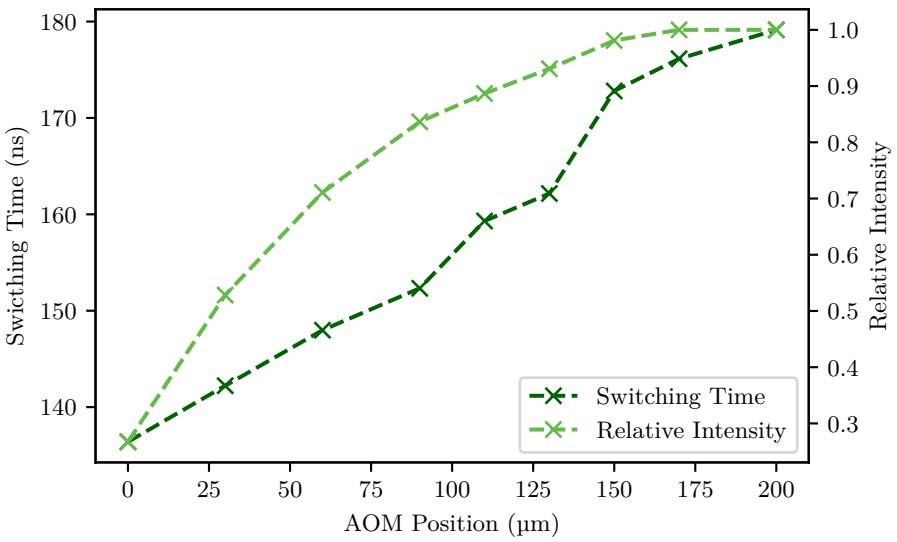

Figure 4.6: Switching time of AOM 1 dependent on its position perpendicular to the laser beam. The position of the AOM is directly related to the distance between the acoustic transducer and the laser beam. The right y-axis gives the corresponding intensities in relation to the absolute intensity of the first diffraction order.

time of all four combinations for the shortest distance between acoustic transducer and laser beam.

The direct comparison of the two AOMs shows, that the switching time for AOM 1 is better for both beam radii. Hence, this AOM is used in all further stabilization processes. Contradicting the assumptions made before, AOM 1 has a faster switching time for the larger beam radius. A possible explanation for this can be found in the corresponding Rayleigh lengths. As explained in Section 3.1.2, the crystal for a similar AOM has a length of $f = 11.5\,\mathrm{mm}$. The measurement results propose that the crystal inside AOM 1 is slightly larger, while the one for AOM 2 is smaller. If the crystal in AOM 1 is larger, the beam radius of the more focused beam expands to larger values while still inside the crystal due to a greater divergence. This is also why the measurements in Figure 4.3 are more stable for AOM 2. Due to the smaller crystal dimensions the position of the focal length plays a less important role.

For this reason a reasonable relation between beam diameter and Rayleigh length has to be found. The beam diameter needs to be small enough to reach short rise times and therefore overall shorter switching times, while the Rayleigh needs to be long enough to ensure a stable value of the switching time for small deviations in the position of the focal point. A suitable solution is found in using lenses with focal length $f = 150\,\mathrm{mm}$ for L3 and L4. The beam waist is then measured to $w_0 = 55\,\mu\mathrm{m}$ which results in a Rayleigh length of $z_\mathrm{R} = 11.1\,\mathrm{mm}$. This setup is used for all further measurements.

Lastly, the influence of the AOM position on the switching time is inspected further. Therefore AOM 1 is adjusted to a position where the first diffraction order is barely visible.

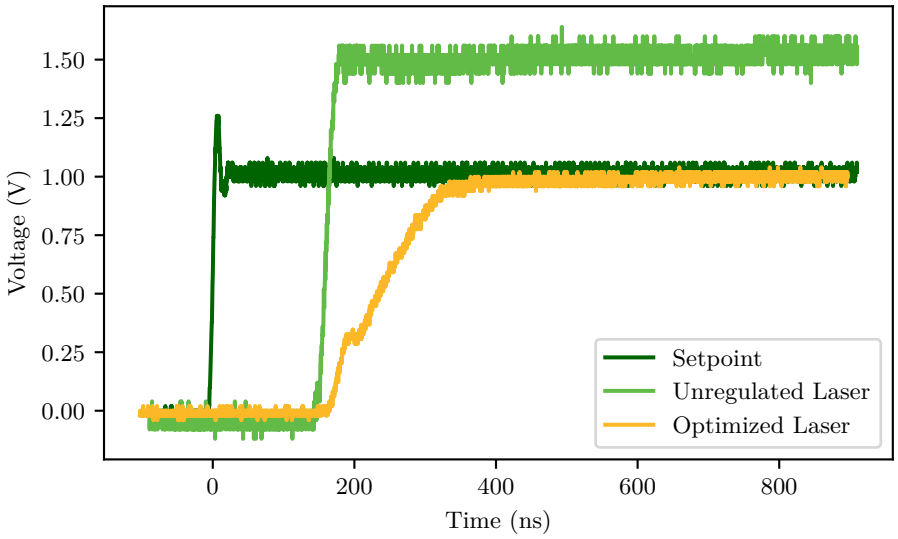

Figure 4.7: Comparision of the unregulated laser pulse with the regulated laser pulse using optimized PID settings. The setpoint is given for reference.

This is done by misaligning the AOM perpendicular to the laser beam, such that no light can pass through it, as it does not meet the opening in the casing anymore. The AOM is then slowly realigned, until the intensity in the first diffraction order can be seen again. This constructs the starting point of the measurement, from which on the AOM is moved in order to increase the distance between the laser beam and the acoustic transducer. The results of this measurement are shown in Figure 4.6. There, a distinct upwards trend of the switching time with the AOM position is visible. A second set of data in the figure shows the corresponding relative intensity values. Those are referenced to the maximum intensity reached in this setup, contrary to the diffraction efficiency, which is referenced to the total laser intensity in accordance with equation (2.20). By using the relative intensity, it is easier to detect when the the diffracted laser beam becomes stable.

The increasing relative intensity indicates, that part of the laser beam is clipped by the aperture for very small distance of the laser beam to the transducer. Additionally, the diffraction does not work properly for short distances from the acoustic transducer due to the distortion of the grating in the near field. The intensity starts to stabilize after the AOM position is corrected by about 200 µm.

4.2 Intensity Stabilization

4.2.1 Optimization Process

In Figure 4.7 the regulated laser pulse is shown in comparison to the unregulated case. Both pulses have approximately the same delay compared to the setpoint. The optimized pulse however has a significantly longer rise time. For the unregulated pulse the rise time is 20 ns, while for the regulated pulse it is approximately 200 ns. The overall regulation

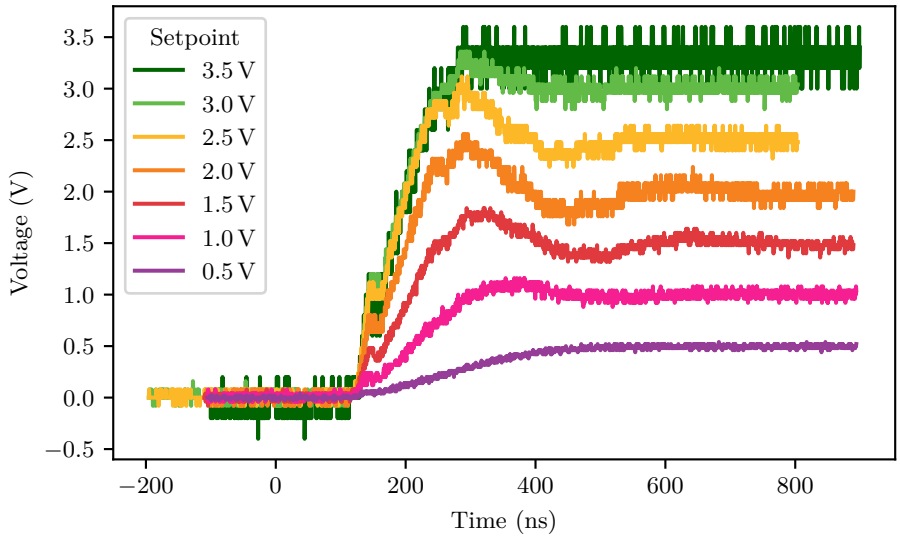

Figure 4.8: Different setpoint amplitudes with the optimized PID settings. The gain of the PID was adjusted fo an amplitude of 3 V.

time is about 400 ns. All settings for the optimized regulation were found starting from the Ziegler-Nichols Method by trial and error [18]. The settings used for the PID controller can be found in Table 4.2. For the measurement, the gain was adjusted to the setpoint amplitude of 1.0 V. Generally, it can be seen, that the regulated laser pulse also has a better signal to noise ratio than the unregulated one.

The delay is only slightly increased for the laser beam in the stabilization loop. This effect can be attributed to the additional distance the signal has to pass, if the control unit is included in the electrical circuit. Since the additional delay is only about 10 ns, it is sufficiently small to be of no importance in comparison to the regulated rise time, which is the tenfold of its original value. Multiple factors contribute to this result. Firstly, adding the control unit into the stabilization circuit limits the bandwidth. While the upper bandwidth limit of the used PID controller is 50 MHz, the typical value amounts only to 10 MHz [30]. Additionally, the output signal of the controller has to be adjusted to the possible input level of the RF driver. This is done using a diode and a potentiometer, slowing the signal down further. Lastly, the rise time is also influenced by the PID settings.

Table 4.2: Settings for the extra slow (XSLI), the slow (SLI) and the fast (FLI) limited integrator as well as the fast limited differentiator (FLD) of the PID controller, which are used for the laser intensity stabilization. The gain has to be adjusted depending on the setpoint. Settings for the Ziegler-Nichols method were obtained in accordance with [18].

Method	XSLI	SLI	FLI	FLD
Ziegler-Nichols	off	off	4	3
Optimized	off	2	10	2

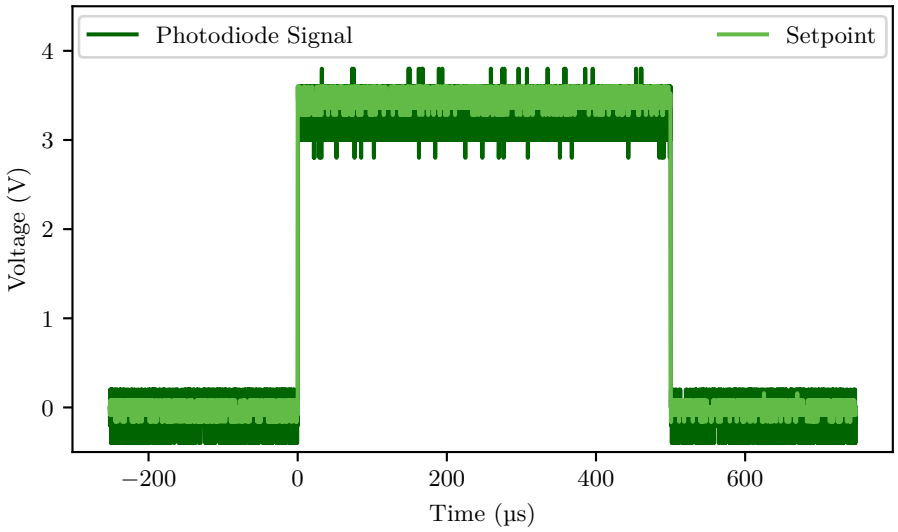

Figure 4.9: Photodiode signal compared to the setpoint signal with PID settings as described in Table 4.2 and a gain adjusted to an amplitude of 3.0 V. The signal on the photodiode is significantly more noisy than the setpoint signal.

Even though settings with a smaller rise time can be found, those solutions are oscillatory, which results in a overall increased stabilization time.

Figure 4.8 shows the consequences of changing the amplitude of the setpoint for a fixed PID gain. For the measurements the gain was adjusted to an amplitude setting of 3.0 V, such that the signal has a slight overshoot with the other parameters as described in Table 4.2. The overshoot increases even more if the setpoint amplitude is fixed to 2.5 V or 2.0 V, and decreases again for smaller amplitude values. The initial rise time of the signal decreases with the amplitude value of the setpoint. For 3.0 V it is equal to 100 ns, while for 0.5 V it is more in the range of 300 ns. The decline of the overshoot and therefore the lack of oscillations for the smaller amplitudes ensures, that the overall stabilization time is approximately constant at a value of 450 ns.

For the larger setpoint amplitude of 3.5 V, the regulation appears to be insufficient as the desired amplitude is not reached with the photodiode signal. However, this only seems to be the case because of the large zoom. As shown in Figure 4.9, the photodiode signal reaches the setpoint value. Compared to the other amplitudes this signal is quite noisy. Together with the increased regulation time, this indicates that the chosen settings are not suitable for larger amplitudes than for which the gain is adjusted. Limitations of the photodiode signal should play no part in this, as the maximum voltage which could be detected was almost 4.5 V.

4.2.2 Influence of Fiber and Cable Length

To examine the influence of an additional optical fiber after the AOM a polarization maintaining single-mode fiber with a length of 5 m is added between L4 and the photodiode to the setup presented in Figure 3.1. As shown in Figure 4.10, the rise times with and

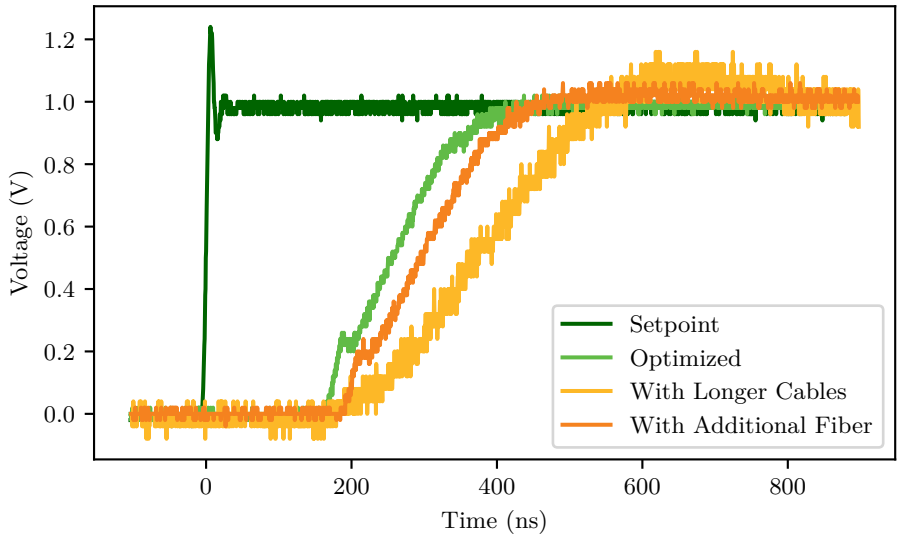

Figure 4.10: Influnce of an additional optical fiber with length 5 m compared to the influence of 4 m longer BNC cables.

without the fiber are equal if the gain is adjusted properly. Nevertheless, a noticeable delay of 25 ns is added to the overall switching time. The expected value for this delay can be calculated using the speed of light in vacuum c_0 as well as the diffraction index of fused silica, which the core of the optical fiber is made of. The diffraction index is $n = 1,452$ [31] for the wavelength $\lambda = 855\,\text{nm}$. The calculated delay is given by

$$t_{\text{delay}} = \frac{5\,\text{m} \cdot 1,452}{299\,792\,458\,\text{m}\,\text{s}^{-1}} \approx 24.2\,\text{ns}, \tag{4.3}$$

which can be considered equal to the measured value for the accuracy of the experiment.

The second effect tested in Figure 4.10 is the influence of longer signal paths in the stabilization circuit. This is realized by extending each input connection with a cable of length 1 m and adding two cables of the same length to the output of the control unit, one before and one after voltage level adaption. Thus, in total 4 m of BNC cable are added to the setup. In this case, the signal is more noisy and the rise time increases significantly. The signal is delayed by 21 ns. The overall switching time is about 200 ns longer than before.

5 Summary and Outlook

In order to control Rydberg quantum gates, actively stabilized laser pulses are required. For this purpose, in this thesis a system to achieve high-bandwidth pulse shaping was realized. The system consisted of an AOM in combination with an electronic feedback loop to control the laser intensity.

The switching time of two different AOMs was examined by modulating a rectangular pulse signal on the RF driver of the respective AOM and comparing it with the corresponding step response of the diffracted laser beam. First, the effect of different beam radii was tested. Since AOM 1 had a generally faster switching time than AOM 2, it was chosen for the later use in the stabilization circuit. The hypothesis, that smaller beam waists equal faster switching times, could only be verified for AOM 2, which has a center frequency of 200 MHz. For AOM 1, which has a center frequency of 80 MHz, this does not hold true. A possible explanation for this effect is offered, if the crystal of AOM 1 is of larger dimension. In this case, the beam radius at the ends of the crystal is significantly larger than in the focal point, which would cause a longer switching time due to a higher rise time. This effect would be most noticeable for a beam with a large divergence. To avoid any possible issues with this, the beam waist was set to $w_0 = 55\,\mu\text{m}$ with a Rayleigh length of $z_\text{R} = 11.1\,\text{mm}$ for the intensity stabilization process. For this parameters the beam radius stays at a sufficiently small level over the length of the AOM crystal to achieve fast, but stable switching times.

Furthermore, the effect of the distance between the acoustic transducer and the laser beam in the AOM was examined. Here, a direct correlation between the distance and the delay could be determined. It was also observed, that the intensity in the first diffraction order depends to a certain extend on the beam-transducer distance. Higher diffraction efficiencies can only be reached if the distance between acoustic transducer and the laser beam is large enough. This is due to a distortion of the diffraction grating in the near-field of the transducer as well as the clipping of the on the AOM casing.

For the measurements with the stabilization circuit a compromise was made with a diffraction efficiency of 50 % and a corresponding switching time of 175 ns. A rectangular pulse was used as a setpoint signal for which the PID controller was optimized to reach a fast laser intensity stabilization. Beginning with the settings obtained via the Ziegler-Nichols method [18], the PID parameters were optimized by trial and error. The final settings, as stated in Table 4.2, generate a stabilization time of 400 ns. This is equivalent to a bandwidth of 2.5 MHz. The stabilization works well for different setpoint amplitudes across a wide range.

Lastly, the influence of longer signal paths and the addition of an optical fiber to the setup were investigated. The optical fiber with a length of 5 m led to the expected delay

of approximately 25 ns, the rise time stayed unchanged. For a measurement with 4 m of additional cable, as expected, more noise was detected on the signal. In this case the rise time increases by 180 ns, resulting in an overall smaller bandwidth. Thus, for an intensity stabilization of high-bandwidth it is necessary to keep the cables as short as possible.

The stabilization bandwidth reached in the scope of this thesis is with 2.5 MHz about a tenth of the ideally desired values between 20 MHz and 50 MHz. This shows, that a simple setup with stock components is not sufficient enough for pulse shaping a laser, which controls Rydberg quantum gates.

This could be further improved by different approaches in the future. One possibility would be to use other types of AOMs. If the propagation length in an AOM crystal was shorter, smaller beam radii could be used, which would decrease the rise time of the AOM. Another reasonable change would be choosing an AOM with a faster sound velocity or different mode-propagation styles. Further, the resonant RF circuit driving the transducer could be optimized to higher bandwidths.

6 Bibliography

[1] T. D. Ladd et al. “Quantum computers”. In: *Nature* 464.7285 (2010), pp. 45–53. DOI: 10.1038/nature08812 (cit. on p. 1).

[2] Daniel Barredo et al. “Synthetic three-dimensional atomic structures assembled atom by atom”. In: *Nature* 561.7721 (2018), pp. 79–82. DOI: 10.1038/s41586-018-0450-2. URL: http://arxiv.org/pdf/1712.02727v1 (cit. on p. 1).

[3] Christian Gross and Immanuel Bloch. “Quantum simulations with ultracold atoms in optical lattices”. In: *Science (New York, N.Y.)* 357.6355 (2017), pp. 995–1001. DOI: 10.1126/science.aal3837 (cit. on p. 1).

[4] Xibo Zhang and Jun Ye. “Precision measurement and frequency metrology with ultracold atoms”. In: *National Science Review* 3.2 (2016), pp. 189–200. ISSN: 2095-5138. DOI: 10.1093/nsr/nww013 (cit. on p. 1).

[5] M. D. Lukin et al. “Dipole blockade and quantum information processing in mesoscopic atomic ensembles”. In: *Physical review letters* 87.3 (2001), p. 037901. DOI: 10.1103/PhysRevLett.87.037901 (cit. on p. 1).

[6] Jaksch et al. “Fast quantum gates for neutral atoms”. In: *Physical review letters* 85.10 (2000), pp. 2208–2211. DOI: 10.1103/PhysRevLett.85.2208 (cit. on p. 1).

[7] L. Isenhower et al. “Demonstration of a neutral atom controlled-NOT quantum gate”. In: *Physical review letters* 104.1 (2010), p. 010503. DOI: 10.1103/PhysRevLett.104.010503 (cit. on p. 1).

[8] T. Wilk et al. “Entanglement of two individual neutral atoms using Rydberg blockade”. In: *Physical review letters* 104.1 (2010), p. 010502. DOI: 10.1103/PhysRevLett.104.010502 (cit. on p. 1).

[9] Harry Levine et al. “High-fidelity control and entanglement of Rydberg atom qubits”. In: *Physical review letters* 121.12 (2018). ISSN: 0031-9007. DOI: 10.1103/PhysRevLett.121.123603. URL: http://arxiv.org/pdf/1806.04682v1 (cit. on p. 1).

[10] Ivaylo S. Madjarov et al. “High-Fidelity Entanglement and Detection of Alkaline-Earth Rydberg Atoms”. In: *Nature Physics* 16.8 (2020), pp. 857–861. ISSN: 1745-2473. DOI: 10.1038/s41567-020-0903-z. URL: http://arxiv.org/pdf/2001.04455v2 (cit. on p. 1).

[11] Berthold Heinrich and Wolfgang Schneider. *Grundlagen Regelungstechnik*. Wiesbaden: Springer Fachmedien Wiesbaden, 2019. ISBN: 978-3-658-26740-7. DOI: 10.1007/978-3-658-26741-4 (cit. on p. 3).

[12] Prof. Jan Lunze. *Regelungstechnik 1*. Berlin, Heidelberg: Springer Berlin Heidelberg, 2020. ISBN: 978-3-662-60745-9. DOI: 10.1007/978-3-662-60746-6 (cit. on p. 3).

[13] Christian Mayr. *Stability Analysis and Controller Design of Local Model Networks*. Wiesbaden: Springer Fachmedien Wiesbaden, 2021. ISBN: 978-3-658-34007-0. DOI: 10.1007/978-3-658-34008-7 (cit. on p. 3).

[14] Karl J. Aström and Tore Hägglund. *PID controllers: Theory, design and tuning*. 2nd ed. Research Triangle Park, Car. du N.: Instrument Society of America, 1995. ISBN: 978-1556175169 (cit. on p. 6).

[15] Serge Zacher. *Drei-Bode-Plots-Verfahren für Regelungstechnik*. Wiesbaden: Springer Fachmedien Wiesbaden, 2020. ISBN: 978-3-658-29219-5. DOI: 10.1007/978-3-658-29220-1 (cit. on p. 6).

[16] Karl Johan Aström and Richard M. Murray. *Feedback Systems: An Introduction for Scientists and Engineers*. Princeton University Press, 2010. ISBN: 978-0691135762 (cit. on p. 8).

[17] Kiam Heong Ang, G. Chong, and Yun Li. "PID control system analysis, design, and technology". In: *IEEE Transactions on Control Systems Technology* 13.4 (2005), pp. 559–576. ISSN: 1063-6536. DOI: 10.1109/TCST.2005.847331 (cit. on p. 8).

[18] J. G. Ziegler and N. B. Nichols. "Optimum Settings for Automatic Controllers". In: *Journal of Dynamic Systems, Measurement, and Control* 64 (1942), pp. 759–768. ISSN: 0022-0434 (cit. on pp. 8, 24, 27).

[19] Wolfgang Demtröder. *Experimentalphysik 1*. Berlin, Heidelberg: Springer Berlin Heidelberg, 2018. ISBN: 978-3-662-54846-2. DOI: 10.1007/978-3-662-54847-9 (cit. on p. 9).

[20] Wolfgang Demtröder. *Experimentalphysik 2*. Berlin, Heidelberg: Springer Berlin Heidelberg, 2013. ISBN: 978-3-642-29943-8. DOI: 10.1007/978-3-642-29944-5 (cit. on p. 9).

[21] Dieter Meschede. *Optik, Licht und Laser*. Wiesbaden: Vieweg+Teubner, 2008. ISBN: 978-3-8351-0143-2. DOI: 10.1007/978-3-8348-9288-1 (cit. on p. 9).

[22] Hans Joachim Eichler, Jürgen Eichler, and Oliver Lux. *Lasers*. Vol. 220. Cham: Springer International Publishing, 2018. ISBN: 978-3-319-99893-0. DOI: 10.1007/978-3-319-99895-4 (cit. on pp. 9, 11).

[23] Markus Werner Sigrist. *Laser: Theorie, Typen und Anwendungen*. Berlin, Heidelberg: Springer Berlin Heidelberg, 2018. ISBN: 978-3-662-57514-7. DOI: 10.1007/978-3-662-57515-4 (cit. on p. 11).

[24] Gooch & Housego. *Datasheet AOMO 3080-122*. URL: https://gandh.com//wp-content/pdfs/3080_122_97_01280_01rD.pdf (cit. on p. 14).

[25] Gooch & Housego. *Datasheet AOMO 3200-1113*. URL: https://gandh.com//wp-content/pdfs/3200_1113_97_02029_05rA.pdf (cit. on p. 14).

[26] ON Semiconductor. *Datasheet 1N4148 Diode*. URL: https://www.onsemi.com/pdf/datasheet/1n914-d.pdf (cit. on p. 15).

[27] Tektronix. *Datasheet MDO3104*. URL: https://download.tek.com/datasheet/MDO3000-Oscilloscope-Datasheet-DE-DE-48G3002011.pdf (cit. on p. 15).

[28] Thorlabs. *Datasheet PDA 10A-EC*. URL: https://www.thorlabs.com/drawings/606607db4f850c41-A73B7AA7-B20C-CE2B-788FAB6A2CE3F2D5/PDA10A-EC-Manual.pdf (cit. on p. 16).

[29] Crystal Technology. *Datasheet 1080-AIFO-1.0*. URL: https://sites.fas.harvard.edu/~phys191r/Bench_Notes/D4/AOM_driver.pdf (cit. on p. 16).

[30] *FALC 110 Manual*. 2013 (cit. on pp. 16, 24).

[31] C. Z. Tan. "Determination of refractive index of silica glass for infrared wavelengths by IR spectroscopy". In: *Journal of Non-Crystalline Solids* 223.1-2 (1998), pp. 158–163. ISSN: 00223093. DOI: 10.1016/S0022-3093(97)00438-9 (cit. on p. 26).